DISCLAIMER:

This document does not meet the
current format guidelines of
the Graduate School at
The University of Texas at Austin.

It has been published for
informational use only.

The Thesis Committee for Wanpeng Liu
Certifies that this is the approved version of the following thesis:

Precise Protein Photolithography (P3) for fabricating High Performance Bioarchitectures Using Silk Fibroin Light Chain as the Photoresist

APPROVED BY
SUPERVISING COMMITTEE:

Supervisor:

Hu Tao

Yaguo Wang

Precise Protein Photolithography (P3) for fabricating High Performance Bioarchitectures Using Silk Fibroin Light Chain as the Photoresist

by

Wanpeng Liu, B.E.; M.S.

Thesis

Presented to the Faculty of the Graduate School of

The University of Texas at Austin

in Partial Fulfillment

of the Requirements

for the Degree of

Master of Science in Engineering

The University of Texas at Austin

May 2017

Acknowledgements

I thank my parents for their unselfish support of my education. Also, I am grateful to Dr. Hu Tao for his guidance, without which this thesis cannot be finished. My collegues, Shaoqing Zhang, and Mike Lee have been a great help for this project. I am very thankful to Dr. Yaguo Wang for providing her reviews for this thesis.

Abstract

Precise Protein Photolithography (P3) for fabricating High Performance Bioarchitectures Using Silk Fibroin Light Chain as the Photoresist

Wanpeng Liu, MSE

The University of Texas at Austin, 2017

Supervisor: Hu Tao

High-resolution fabrication platforms using materials from biological precursors have been proposed as feasible routes not only for sustainable bionanomanufacturing, but also for creating organic devices to interface and interact with biological systems. In this study, silk fibroin, as a biomaterial, has been used as a photoresist via chemical conjugation with photocrosslinkers. The Achilles heel of natural silk fibroin based resists is the inevitable wide molecular weight distribution (ranging from a few tens to a few hundreds of kDa). Such essential issue hinders their practical uses in the semiconductor industry where reliability and repeatability are paramount. To solve such an issue, we report on wafer-scale high resolution patterning of bio-microstructures using silk fibroin light chain (L-fibroin or LC) as the resist material. The L-fibroin fragments with the well-defined molecular weight were successfully isolated from the integral silk fibroins consisting of both heavy and light chains. Under facile biochemical modification, the L-fibroin

photoresist is synthesized via conjugating commercial photocrosslinkers as crosslinking sites in the presence of ultraviolet light. To explore the characteristics and to explain the mechanism of resolution, roughness and etch resistance of the as-prepared patterns, we use the scattering-type scanning near-field microscope (s-SNOM) which provides direct imaging and chemical identification of the thin protein layers at the nanoscale. The enhanced patterning resolution, the improved etch resistance and the inherent biocompatibility of such protein-based photoresist provide new opportunities in fabricating large scale biocompatible functional microstructures.

Table of Contents

List of Figures ix

Chapter 1: Introduction 1

Chapter 2: Principles of s-SNOM 5

Model of tip–sample interaction 6

Background-scattered light 8

Chapter 3: Experimental Section 10

Synthesis and purification of photosensitive proteins 10

Synthesis of photosensitive L-Fibroin (UV-LC) 10

Photolithography 12

Fourier transform infrared spectroscopy (FTIR) 13

Scattering-type near-field optical microscopy (s-SNOM) 14

Young's Modulus measurement 15

SDS-PAGE analysis 15

Bioactivity test of silk protein photoresist 16

Cell culture 16

Immunofluorescence assay 16

Chapter 4: Results and Discussion 18

Fabrication of the UV-Silk and UV-LC Micropatterns 18

Characterization of the UV-Silk and UV-LC Micropatterns 25

Crooslinking Mechanism Analysis of the Micropatterns 30

Etching Resistance Measurement and Analysis of the Micropatterns 37

Biocompatability and Cell Culture Analysis of the Micropatterns 41

Chapter 5: Conclusion 44

References 45

List of Figures

Figure 1: Schematic diagram of s-SNOM equipment. 6

Figure 2: Analytical modelling of s-SNOM represents the probe tip by a sphere, and the interaction with the sample by an induced 'image' dipole.....7

Figure 3: Step by step schematics of fabricating UV sensitive silk fibroin proteins solution.....12

Figure 4: Synthesis of the UV-reactive silk L-fibroin (UV-LC) and the result of photolithography using UV-LC as a negative resist. B. mori cocoons (a) are degummed for 60 minutes to obtain silk fibroin (b), and the L-fibroin (c) is then separated from the silk fibroin using formic acid; (d) photoactive L-fibroin (UV-LC precursor) is obtained by conjugating IEM to the L-fibroin; (e) by adding the photoinitiator (Irgacure 2959), the UV-LC resist can be synthesized; (f) Photolithography using UV-LC resist; (g) Optical images of the fabricated patterns (Linewidth: 5 μm, zoom-in image) shows that UV-LC has better lithographic performance than UV-Silk30. Scale bar: 50 μm. (h) Dark-field stereomicroscopic photograph of double immunofluorescence staining with nestin (green fluorescence) and nuclear staining (blue DAPI staining) of fetal neural stems cells that were guided to be cultured on a micropatterned UV-LC resist (dash line) on a silicon substrate. Scale bar: 100 μm. 20

Figure 5: Solubility measurement of silk fibroin proteins under 10, 30, 60, 90 minutes degumming time in different solvents including water, water with salts, TFE and DMSO. 21

Figure 6: (a) SDS-PAGE analysis of the silk fibroin protein with different degumming time, MaSp1: recombinant spider silk protein; (b) SDS-PAGE analysis of the silk fibroin protein and L-Fibroin from reference [18]. 23

Figure 7: Schematic comparison between structures of UV-LC and UV-Silk (including both UV-Silk30 and UV-SilkHTP) precursor, where UV-Silk30 has longer protein chains than UV-HTP. UV-LC contains only L-fibroin. 24

Figure 8: Characterization and analysis of patterns fabricated by protein photolithography using different types of silk-based materials (e.g. UV-Silk30, UV-SilkHTP, and UV-LC. Morphological characterization (using an optical microscope and AFM, scale bar: 200 μm) of micropatterns fabricated by protein photolithography using UV-Silk30, UV-SilkHTP, and UV-LC. It shows that the UV-LC can achieve better resolution and surface smoothness than UV-Silk30 and UV-SilkHTP. ……..25

Figure 9: (a) AFM image of 3D view of the surface of silk fibroin protein under 30 minutes degumming time; (b) AFM image and SNOM images of both absorbance and reflection spectrum of the surface of silk fibroin protein under 30 minutes degumming time; (c) Microscope and AFM images of the silk fibroin protein under 30 minutes degumming time to compare the influence of underlying substrate. 28

Figure 10: Quantitative analysis of resolution (a) and surface roughness (b) of micropatterns fabricated using various UV-Silk and UV-LC. The result is consistent with the observations from optical and AFM images...29

Figure 11: FTIR spectroscopy on the silk fibroin proteins confirms the presence of both amide I/II/III peaks from native silk fibroin proteins, in addition to stretching vibrations at 1720 cm-1 (ester carbonyl C=O) and 1630 cm-1 (vinyl C=C), and vibrations at 1160 cm-1 (CH3) from the methacrylate substituent. 33

Figure 12: Structural characterization of the UV-Silk and UV-LC using FTIR and s-SNOM. (a) Schematic of ATR-FTIR setup, where the sample is illuminated from the back of the ATR crystal; (b) FTIR spectrum of IEM, silk fibroin protein, UV-silk, and UV-LC. The peaks vanish in the UV-Silk and UV-LC, indicating the binding of IEM on silk fibroin and L-fibroin; (c) Schematic of the s-SNOM system. An infrared laser is focused onto the AFM tip, and the scattered signal is collected by the detector; (d) & (e) IR nano-imaging and absorbance (acquired by s-SNOM measurement performed at 1,635 cm-1) of UV-Silk30, UV-Silk90, UV-SilkHTP and UV-LC with various exposure time. The disappearance of the absorbance with increasing exposure time indicates the increasing crosslinking degree of IEM until about 90 s, after which time all the available IEM active conjugated acrylate group sites are crosslinked. 37

Figure 13: Etching rate measurements and schematic structures of various UV-Silk and UV-LC. (a) Etching rate measurement of the UV-Silk30 and UV-LC with increasing exposure time. The etching rate of UV-LC decreases faster than the UV-Silk30 with increasing exposure time but reaches a constant rate that is higher than UV-Silk30; (b) Etching rate comparison between various UV-Silk (including both UV-Silk and methanol treated UV-Silk) and UV-LC at two exposure times (20s and 120s). All the samples with 20 s exposure times have larger etching rate than the samples with 120 s exposure times. UV-Silk has an increasing etching rate with increasing degumming time because the mechanical strength is better with longer chain length. UV-LC has slightly less etching rate because its highly defined molecular structure help form better crystalline structure; (c) Young's modulus of UV-Silk and UV-LC. It shows the similar trend with the data of etching speed, where the largest Young's modulus value corresponds to slower etching rate; (d) Schematic structure and the corresponding etching rate of the photocrosslinked UV-Silk and UV-LC with 20 s exposure time and UV-Silk30 exposed for 120 s. For UV-Silk30, the etching rate decreases with longer exposure time because of the increased crosslinking degree. With the same exposure time, the etching rate increases with increasing degumming time because of the shorter chain length, and thus less mechanical strength. With 20 s exposure (partially crosslinking) UV-LC has less etching speed because its highly defined molecular structure helps it form better IEM-induced crystalline structure. 41

Figure 14: (a) and (b) Bioactivity detection (ELISA) of pure silk resist and HRP enzyme doped silk resist (which turns blue) after UV exposure and pattern development. The bioactivity test shows that as-prepared patterns possess bioactivity of embedded biological molecules to some extent during silk light chain protein photolithography; (c)-(g) Double immunofluorescence staining with nestin (green fluorescence) and nuclear staining (blue DAPI staining) of fetal neural stem cells cultured on micropatterns made of silk light chain photolithography. 43

Chapter 1: Introduction

Precise patterning of micro- and nano-structures using polymer-based biomaterials has wide applications including drug release, degradable implants, tissue engineering, and regenerative medicine [1-4]. High-resolution fabrication platforms using materials from biological precursors have been proposed as feasible routes not only for sustainable bionanomanufacturing, but also for creating organic devices to interface and interact with biological systems. In this context, natural silk proteins obtained from cocoons of the silkworm *Bombyx mori* provide "green" alternatives to synthetic materials with advantages such as superior mechanical properties (strength and toughness), outstanding biocompatibility and biodegradability, and controllable water-solubility and degradation rate [1, 5-7].

Natural silk fibers from *Bombyx mori* cocoons exist in a self-assembled fibrous configuration, in which a mechanically robust protein - fibroin (~ 75%, w/w) comprises the core, surrounded by a glue protein - sericin (~ 25%, w/w) [8]. Due to the presence of a high content of hydrophilic amino acids (~70%), sericins are soluble in water. As sericins are involved in inducing allergic and immunological reactions, all sericin is able to be removed from fibroin intended and leaving fibroin protein for further applications. Silk fibroin, the structural protein of *Bombyx mori* silk fibers, is a large protein macromolecule constructed of more than 5,000 amino acids and insoluble in many solvents including water. Silk fibroin is comprised of both crystalline (~66%) and amorphous (~33%) regions. The crystalline region of fibroin is composed of repeating units of the amino acids glycine (G), alanine (A), and serine (S), typically $[G\text{-}A\text{-}G\text{-}A\text{-}G\text{-}S]_n$ and form β-sheet structures in the spun fibers, which are responsible for the mechanical properties.

Recently, several industries, such as photonics, implantable bioelectronics, and nanostructured scaffolds, rather than conventional application such as hydrogels, fibers, particles or films, have developed and utilized pure fibroin and sericin or their blends with other materials. The increasing demand for silk thus requires innovative approaches to develop multi-scale fabrication of silk with manufacturing scalability. To date, several techniques, such as imprinting, molding, electrospinning, embossing, inkjet printing, and photolithography have enabled the development of a variety of material formats including hydrogels, fibers, particles, and films using fibroin or sericin as well as their blends with other materials [3, 9, 10]. Photolithography, in particular, remains one of the most appealing techniques for scalable biomanufacturing as it is CMOS-compatible and can rapidly fabricate high fidelity micro-/nano-patterns in parallel – in contrast, scanning-probe lithography and electron beam lithography for biomanufacturing use serial manufacturing techniques [11-15].

Photolithography can pattern proteins either directly or indirectly. The application of optical lithography to proteins has been relatively uncommon and primarily based on indirect methods in which proteins are attached to functionalized surfaces. In this method, light-induced activation, deposition or passivation using different types of chemistry are employed to form patterns, followed by covalent protein immobilization. Comparing to the indirect method, the method to directly pattern proteins inherently requires photoreactive materials as photoresists. Examples of the direct method include photoreactive derivatives of biotin, elastin-like proteins, and non-canonical amino acids incorporated via site-specific and residue-specific techniques. In particular, patterning of silk microstructures using UV-photolithography has been successfully demonstrated where either silk fibroin or sericin was chemically modified to be photoreactive and then served as the photoresist [16, 17]. Cell culture studies have been conducted to verify the biocompatibility of silk protein

resists after the chemical modification and lithographic process [16, 17]. Though very promising, compared to their commercial counterparts based on synthetic polymers, current silk protein resists still suffer from issues such as relatively low resolution and pattern contrast in terms of lithographic patterns, mainly due to the inevitable wide molecular weight distribution (ranging from a few tens to a few hundreds of kDa for both silk fibroin and sericin proteins) during the degumming process for protein extraction [18]. Such limits hinder their practical use in precision biopatterning and the semiconductor industry where reliability and repeatability are paramount. Proteins with more uniform molecular structures (such as well-defined chain lengths and molecular weights) and preferably more active group sites for further functionalization have yet to be explored for high-performance protein-based photolithography.

In this study, we report a precise protein photolithography (P3) for high-performance biopatterning using the well-defined silk fibroin light chain as the basic resist material. Silk fibroin is mainly composed of two components, namely heavy chain (H-fibroin, ~ 85%, w/w) and light chain (L-fibroin, ~ 15%, w/w), which are linked by a single disulfide bond between Cys-c20 of H-fibroin and Cys-172 of L-fibroin [19-21]. The H-fibroin portion has a primary structure formed by highly repetitive sequences of GAGAGS, GAGAGY, and GAGAGVGY, which are mainly hydrophobic resulting in the hydrophobic property of silk fibroin. The secondary structure is mainly β-sheet with antiparallel assembly resulting in enhanced stability, crystallinity, and mechanical properties in the fibers. Compared to silk sericin, fibroin proteins and its heavy chain portion, L-fibroin has a well-defined molecular weight of ~ 26 kDa [22]. In addition, L-fibroin has a more undifferentiated and hydrophilic amino acid composition resulting in the facile chemical modification. Separation procedures of the heavy chain and light chain from silk has been attempted by many methods such as chromatographic separation using Sephadex resins

followed by SDS-PAGE for the light chain and DEAE-cellulose for the heavy chain, although both approaches are complicated and produce inadequate quantities of the isolated components for scale up [23-25]. A simple method of separating silk fractions was employed using a formic acid treatment which partially releases predominately the light chain fragment. Without losing the advantages of integral silk protein, the light chain can provide higher resolution, more mechanical stability, hydrophilic character, degradation, and cell adhesion than either the mixed system or the heavy chain alone. Consequently, it can fabricate large-scale biocompatible functional micro- and nano-structures based on the light chain protein photoresist.

Chapter 2: Principles of s-SNOM

Scattering-type near-field optical microscopy (s-SNOM), also referred to as 'apertureless' near-field optical microscopy, offers ultrahigh resolution independently of the wavelength. Better resolution is possible with a different type of optical probing tip, the so-called 'apertureless' design. In a typical s-SNOM setup (Figure 1), an external beam of IR laser is focused on the a sharply tipped needle (AFM tip). The tip has two distinguishable optical functions:

1) To intercept and reradiate incoming light like an optical antenna;
2) To supply a concentrated longitudinally polarized optical field at the tip apex to probe the optical response of a nearby sample material. The resolution is given by the tip's curvature radius.

Due to the electromagnetic nature of the laser, the electrical field will accumulate at the apex of the tip which is thus enhanced and polarizes the samples. This field enhancement together with a modulation of the tip-to-sample distance allows us to observe a localized light scattering. The scattering phenomenon then happens between the tip and the sample if their distance is close (a few hundred nanometers). The scattered signal is subsequently reflected from the tip and collected in the optical detector. The theoretical resolution of the optical signal is as small as the radius of the apex of the AFM tip since the optical enhancement is confined to the apex of the tip on the scale of its curvature (Ocelic, Huber, & Hillenbrand, 2006). Therefore, this technique can overcome diffraction limit of classical optical microscope and enable nanoscale measurement.

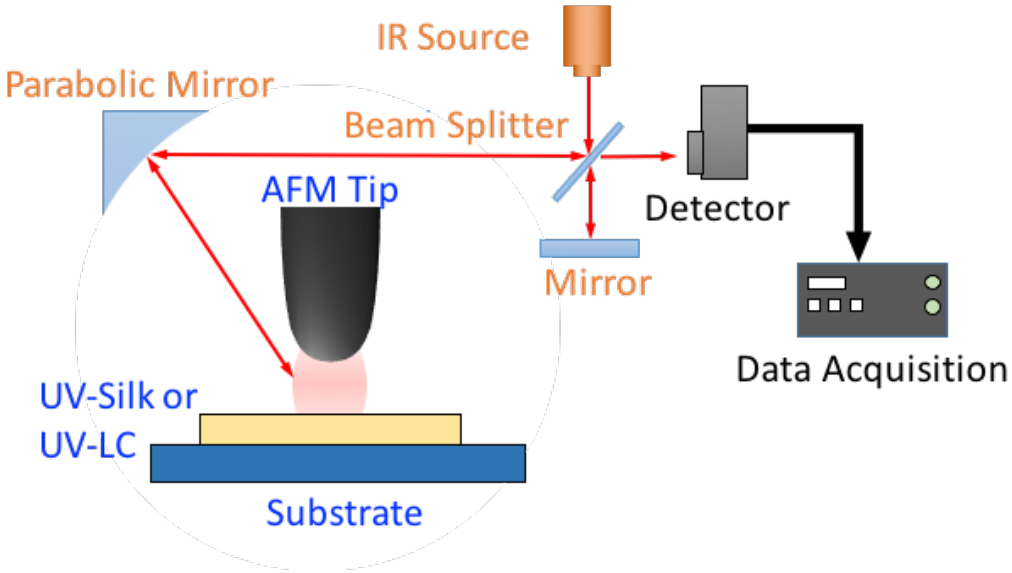

Figure 1: Schematic diagram of s-SNOM equipment.

MODEL OF TIP–SAMPLE INTERACTION

A simple analytical model was presented to describe the electromagnetic interaction between point dipoles. It represents the molecules or small clusters, and for the needs of s-SNOM, the probe tip and nanoscopic samples, both approximated as polarizable spheres. By assuming the probe diameter to be much smaller than the wavelength, such model can describe the probe diameter to be much smaller than the wavelength. This assumption is applicable for the ultra-sharp s-SNOM tip and working with longer wavelengths in the infrared.

According to the quasi-electrostatic theory, the theory assumes the scattering probe to be a polarizable sphere (radius a, polarizability α), at distance $z = r - a$ above the sample (Figure 2). The materials of sample should be a dielectric or metallic half space with complex dielectric number. When applying an electric field E perpendicular to the

sample surface (Figure 2), the sphere becomes polarized with dipole moment $p = \alpha E$. The electric field of the induced probe dipole,

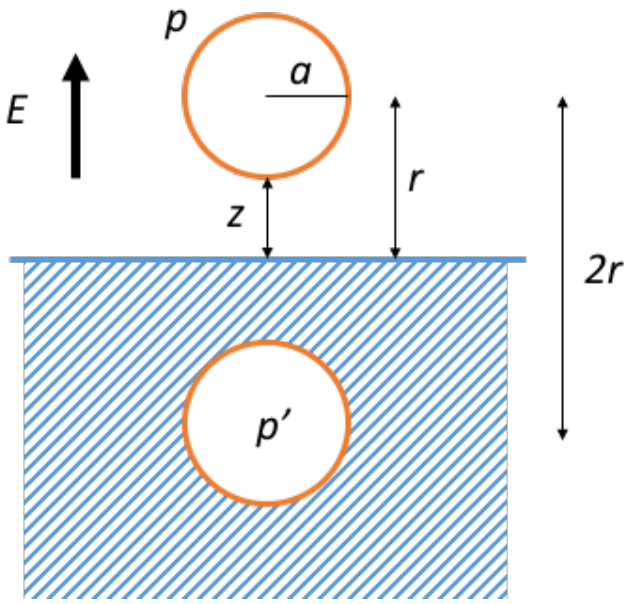

Figure 2: Analytical modelling of s-SNOM represents the probe tip by a sphere, and the interaction with the sample by an induced 'image' dipole.

$$E_{dipole}(r) = \frac{p}{2\pi r^3}$$

induces surface charges in the sample. Their fields can be described as $p' = \beta p$, $\beta = (\varepsilon - 1)/(\varepsilon + 1)$ located inside the sample at a distance $2(z + a)$ from the probe dipole. The incident field at the probe dipole is enhanced by such field so that in the electrostatic limit the actual probe dipole moment is modified:

$$p = \alpha\left(E + \frac{p'}{16\pi(z+a)^3}\right) = \left(\frac{\alpha}{1 - \frac{\alpha\beta}{16\pi(z+a)^3}}\right)E$$

Since the total field of the probe-sample system is a superposition both probe and fields, the coupled system the effective polarizability is obtained:

$$\alpha_{\perp}^{eff} = \left(\frac{\alpha(1+\beta)}{1 - \frac{\alpha\beta}{16\pi(z+a)^3}} \right)$$

which is strongly enhanced at short distances $z \leq a$.

BACKGROUND-SCATTERED LIGHT

In s-SNOM system, the scattering probe tip is usually illuminated through a free-space focusing lens. Other types of illumination are either through waveguides (coaxial or tetraeder) or through the sample. In any case a relatively large area of λ^2 or more, including the shaft of the tip and the sample, is illuminated. This is the source of so-called background scattering σ^b which adds to the pure near-field scattering signal σ.

One difficulty in the s-SNOM setup is the elastic scattering background between the tip and sample, as well as the background from the environment. It is necessary to suppress this background or to correct it by a subtraction procedure at this situation. A suppressing technique was carried out to introduce into the near-field optical microscopy, where the tip–sample distance was modulated such that a demodulation of the scattered signal could enhance the near-field contribution over the background. As far as subtraction methods are concerned the near-field and background scattering add coherently, because both are generated from the same driving field in intimate proximity. This means that any subtraction procedure has to work on the level of light fields, at which the superposition principle of electromagnetics applies, in contradistinction to the level of light intensities where interference can cause trouble.

In this study, a technique called Pseudo heterodyne detection is invented (Ocelic, Huber, & Hillenbrand, 2006) to suppress the background signals. In its setup, another

reference beam of laser, originated from a beam splitter of the same laser is directed into the optical detector with the scattering beam. The reference beam is phase modulated by a Michelson Interferometer to create modulated interference between the reference beam and the scattering beam. This modulation allows recovery of the pure near-field signal of the s-SNOM if the overall signal is demodulated at higher harmonics. This phenomenon is attributed to the non-linear nature of the dependence of tip scattering on the tip-sample distance. It is further proved that the demodulated detector signal amplitude is related to the reflectivity property of the sample surface, while the signal phase is related to the absorption. In consequence, both reflection and absorption can be measured.

Chapter 3: Experimental Section

SYNTHESIS AND PURIFICATION OF PHOTOSENSITIVE PROTEINS

60 minutes degummed silk fiber was weighed and dispersed in 98 – 100% formic acid at a range of concentrations (0.01 – 8% w/v) for 30 min. The mixture was then centrifuged at 4,000 rpm for half an hour to sediment the undissolved material. The supernatant was filtered using glass fiber filters to remove any remaining suspended particles/ fibers. Then, the soluble fractions were left under a flow of air at room temperature to evaporate to constant weight. Note that the degumming conditions significantly affect the performance of UV-Silk resist but have much less effect on UV-LC resist.

Silk fibroin proteins were prepared using the established purification protocols. *B. mori* cocoons were boiled for 30 min in aqueous 0.02 M Na_2CO_3 (Sigma-Aldrich, USA) and then rinsed for 3 × 30 min in distilled water to remove the Na_2CO_3 and sericin. The degummed cocoons were allowed to dry for more than 12 h and then subsequently dissolved in 9.3 M LiBr (Sigma-Aldrich, USA) solution at 60 °C for 4 h. The solution was dialysed for 2 days in distilled water using Slide-a-Lyzer dialysis cassettes (MWCO 3,500, Pierce, USA). The solution was centrifuged for 2 × 20 min at 18,000 r.p.m. The concentration was determined by measuring a volume of solution and the final dried weight.

SYNTHESIS OF PHOTOSENSITIVE L-FIBROIN (UV-LC)

The L-fibroin photoresist was synthesized via chemical conjugation between L-fibroin and photocrosslinkers (2-Isocyanatoethyl methacrylate, IEM) in an anhydrous environment. L-fibroin was suspended at 1% (w/v) in a solution of 1M LiCl/DMSO and stirred at 65 ºC in a dry N_2 atmosphere for 40 minutes. Immediately after, the IEM was

added at a stoichiometric equivalent to reactive hydroxyl-containing amino acids and reacted for 5 hours at 65 ºC. The product was precipitated out, centrifuged, washed and freeze-dried, sequentially. For comparison, silk fibroins under 10, 30, 60, 90 minutes degumming time, as well as silk HTP (high temperature and pressure) were prepared and synthesized to be photoreactive following the similar procedure in the supplementary information.

Silk fibroin photoresist was synthesized via chemical conjugation between silk fibroin protein and the reactive isocyanate group of 2-isocyanatoethyl methacrylate (IEM) in an anhydrous solvent system to prevent premature isocyanate reaction. Lithium chloride, silk fibroin protein, and all glassware were thoroughly dried prior to use (Figure 3). Silk fibroin protein was suspended at 1% (w/v) in a solution of 1M LiCl/DMSO and stirred at 65 ºC in a dry N_2 atmosphere for 40 minutes, at which point no solids remained suspended in solution. Immediately after, the reagent IEM was added at a stoichiometric equivalent to reactive hydroxyl-containing amino acids. The reaction was allowed to proceed to completion for 5 hours at 60 ºC. The product after the reaction was precipitated out into cold ethanol, and centrifuged. The solid product was then washed with a mixture of cold ethanol/acetone and centrifuged three times. Finally, lyophilization for 48 hours yielded a pure white powder.

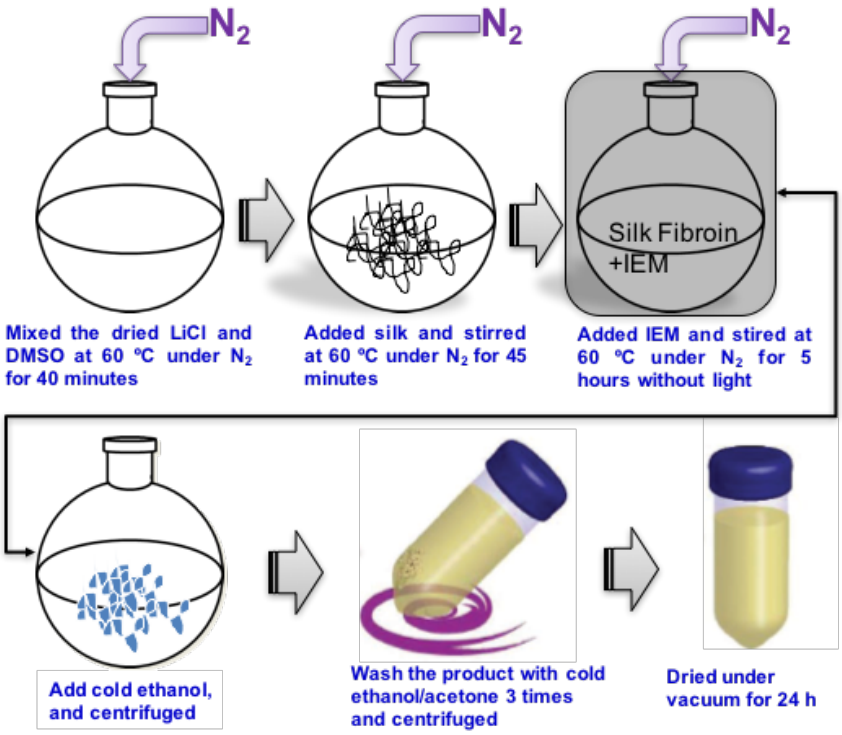

Figure 3: Step by step schematics of fabricating UV sensitive silk fibroin proteins solution.

PHOTOLITHOGRAPHY

Microscale patterns of fibroin were fabricated using photolithography. A solution of 2% (w/v) photoresist was prepared using 1,1,1,3,3,3-hexafluoro-2-propanol (HFIP, Sigma Aldrich, St. Louis, MO) as a solvent and 0.5% (w/v) of Irgacure 2959 (Sigma Aldrich, St. Louis, MO) as a photoinitiator. The principle of solvent selection was discussed in the supplementary information. The photoresist solution was then cast at 0.5 mg per substrate. Contact photolithography was conducted using a photomask under a UV exposure (Lumen Dynamics OmniCure 1000, 320–500 nm filter). The unexposed and uncrosslinked protein photoresist was developed using deionized water (18.2 MΩ•cm) for 2 hours followed by copious rinsing with deionized water and ethanol. Substrates with the developed protein patterns were then dried in a gentle stream of dry N_2.

FOURIER TRANSFORM INFRARED SPECTROSCOPY (FTIR)

Fourier transform infrared spectroscopy (FTIR) is a well-established tool for chemical composition identification by mapping the material absorption of light as a function of wavelength in the infrared range. FTIR shines a broad band light on the sample, and use a moving mirror as the reference arm to interfere with the signals. Since different wavelength is interfered at different frequency, the single wavelength absorption can be recovered via demodulation of the signal specific to that wavelength by using the Fourier Transform of the raw data.

FTIR allows high throughput spectroscopic measurement through mapping absorption for a broad range of wavelength in a single scan. It is significant for high throughput measurements since spectroscopic measurement, especially in the infrared region can be very noisy due to its high sensitivity to the background environment. With high speed FTIR, tens, or even hundreds of measurements can be taken repeatedly, eliminating the effect of random fluctuations in the environment (Ferraro, J. R. 2012).

Two major operation modes of FTIR are presented: the transmission mode and the reflection mode. In transmission mode, the sample is simply positioned in the optical path of the light source, and detector is in the downstream of the optical path. In the reflection mode, the light source is incident on a Germanium crystal, and reflected backward the detector. At the spot where the reflection happens, there is a beam of evanescent wave escape from the other side and is incident on the sample, which is pushed tightly against the Germanium crystal. The evanescent wave penetrates through the sample surface for about 2 μm and is scattered back. The scattered light then carries information of the sample surface. The reflection mode FTIR is widely used for characterization of thin films because it eliminates the effect of the substrate.

In this study, to confirm the methacrylate conjugation, FTIR was conducted on unmodified silk fibroin proteins and L-fibroin film using a Nicolet iS10 FTIR spectrometer. Cast films (5.0 mg) were analyzed in attenuated total reflectance (ATR) mode using a Ge ATR crystal, and data was collected between 4000 – 1000 cm^{-1}, for 32 scans at a resolution of 1 cm^{-1}.

SCATTERING-TYPE NEAR-FIELD OPTICAL MICROSCOPY (S-SNOM)

Scattering Scanning Near-field Optical Microscope is a versatile technique in chemical and structural material characterization. s-SNOM set-up employing a tunable single line IR quantum cascade laser (1,450 to 1,750 cm^{-1}) for tip illumination (Figure 1). During instrument operation, the light backscattered from the tip is collected and analyzed with a Michelson interferometer operating in pseudo-heterodyne mode. The laser was attenuated to ~10 mW such that the detector yields a nominal signal of 1.5 V. The AFM was operated in tapping mode with 65 nm tapping. Gold-coated AFM tips with about 250 kHz resonance (Tap300G-B-G, budgetsensors.com) were used to optimize the IR near-field signal. The IR signal was detected simultaneously with AFM signals. The IR signal used for analysis in this work was measured by a pseudo-heterodyne technique and a lock-in amplifier. Such amplifier was set at the second and third harmonics of the tapping frequency which provides both reflection and absorption that are (mostly) free of background. Both amplitude and phase information is collected. The near-field interaction leads to a phase spectrum that resembles a familiar molecular absorbance band, while the near-field amplitude spectrum acquires a dispersive line shape similar to a far-field reflectivity spectrum.

In this study, due to the vibration of tip, the real optical signal is modulated at the tip vibrating frequency. Since the optical signal dependence on the tip-sample distance is

non-linear, the overall signal carries background information at higher harmonics. In other words, if the overall signal is demodulated with multiples of the tip vibration frequency, background information is obtained and influence the final results. With increasing signal order, the signal is more independent of background, but the signal strength is thus lower, which yields low signal-to-noise ratio (SNR). With common polymers (not as reflective as doped silicon), the second order optical signal is often used for characterization. Also, to increase the SNR, the power is reduced by positioning a Germanium optical attenuator in the reference arm. The reduction is about 75%.

YOUNG'S MODULUS MEASUREMENT

The Young's Modulus is measured by the Force-Distance Spectroscopy module of a commercial AFM (NT-MDT, Russia). The AFM records the applied Z-movement of the cantilever and the real deflection of the tip. The Young's modulus can then be calculated (given a simple model of the AFM tip). For all the measurement, a single ARROW-NCPT tip (NanoWorld, Switzerland) is used and the tip radius is assumed to be 25 nm according to the specification.

SDS-PAGE ANALYSIS

The protein concentration of dialyzed silk solutions was estimated using the Bradford protein assay. Sample buffer (Laemmli 2x; pH 6.8), containing 10% of 2-mercaptoethanol and 0.004% bromophenol blue was modified according to reported methods by adding urea and SDS to achieve a final level of 8 M and 10%, respectively. All samples were diluted with this modified sample buffer (pH 6.8) in a volumetric ratio of 1:1 and were denatured by heating in a water bath at 50 °C for 10 min. All samples were centrifuged at 2,000 rpm for 30 s and were then loaded in the polyacrylamide gel alongside

protein markers. Gel electrophoresis was performed in running buffer (pH 8.3) containing SDS (0.1%), trizma base buffer (25 mM), glycine 192 (mM), and HCl (to adjust pH) at a fixed voltage of 120 V until all samples approached the bottom of the gel.

BIOACTIVITY TEST OF SILK PROTEIN PHOTORESIST

HRP (Sigma Aldrich) was mixed with aqueous UV-LC solution to a final concentration of 0.2 unit ml-1. The HRP-containing UV-LC solution was spin-coated onto a quartz substrate to a thickness of 100 nm, and floor UV exposure treatment using the previously described method. After developing with the Li/DMSO developer solvent, the remaining resist was exposed to 3,3′,5,5′-tetramethylbenzidine (TMB) solution (Sigma Aldrich) to test the activity of the HRP stabilized within the UV-LC resist.

CELL CULTURE

Human fetal neural stem cells were subcultured when they were over 90% confluent. Cells were plated in a medium consisting of DMEM/F12 (GIBCO), 10% fetal bovine serum (GIBCO), penicillin/streptomycin (GIBCO), and 3.5 mM glucose (Sigma), supplemented with B27 (GIBCO), 10 ng/ml EGF (Invitrogen), and 10 ng/ml FGF2 (Invitrogen). Cells were maintained at 37°C in humidified air with 5% CO_2.

IMMUNOFLUORESCENCE ASSAY

For cell culture staining, the cultures were fixed in 4% PFA in PBS for 15 min at room temperature. Cells were first washed three times by PBS and then pretreated in 0.1% Triton X-100 in PBS for 15 min, followed by incubation in 4% normal donkey serum, and 0.1%Triton X-100 in PBS for 30 min. Primary antibodies (1^{st} ab source rabbit, nestin abcom) were incubated with cultures overnight at 4°C in 2% normal donkey serum, and 0.1% Triton X-100 in PBS. After additional washing in PBS, the samples were incubated

with appropriate secondary antibodies (2nd ab donkey anti rabbit 488 flour) conjugated to Alexa Fluor 488 Alexa Fluor.

Chapter 4: Results and Discussion

Fabrication of the UV-Silk and UV-LC and Micropatterns

Figure 4 illustrates the material synthesis, functionalization, and photolithographic results of UV-reactive silk L-fibroin (UV-LC) resists. The *Bombyx mori* silkworm cocoons were first cut into small pieces and degummed for 60 minutes to remove sericin using a previously reported process [26] (Figure 4a & 4b). Formic acid was used to break the covalent disulfide bonds between H-fibroin and L-fibroin, and to separate silk fragments based on their different solubilities in formic acid without causing severe protein degradation [27, 28]. The soluble fractions (i.e., L-fibroin) were harvested and air-dried (Figure 4c). The L-fibroin was modified to be photoreactive by conjugating a photoreactive reagent of 2-isocyanatoethyl methacrylate (IEM) to L-fibroin's side groups, yielding a photocrosslinkable UV-LC precursor (Figure 4). The UV-LC precursor was then dissolved in 1,1,1,3,3,3-hexafluoro-2-propanol (HFIP, Sigma Aldrich, St. Louis, MO).

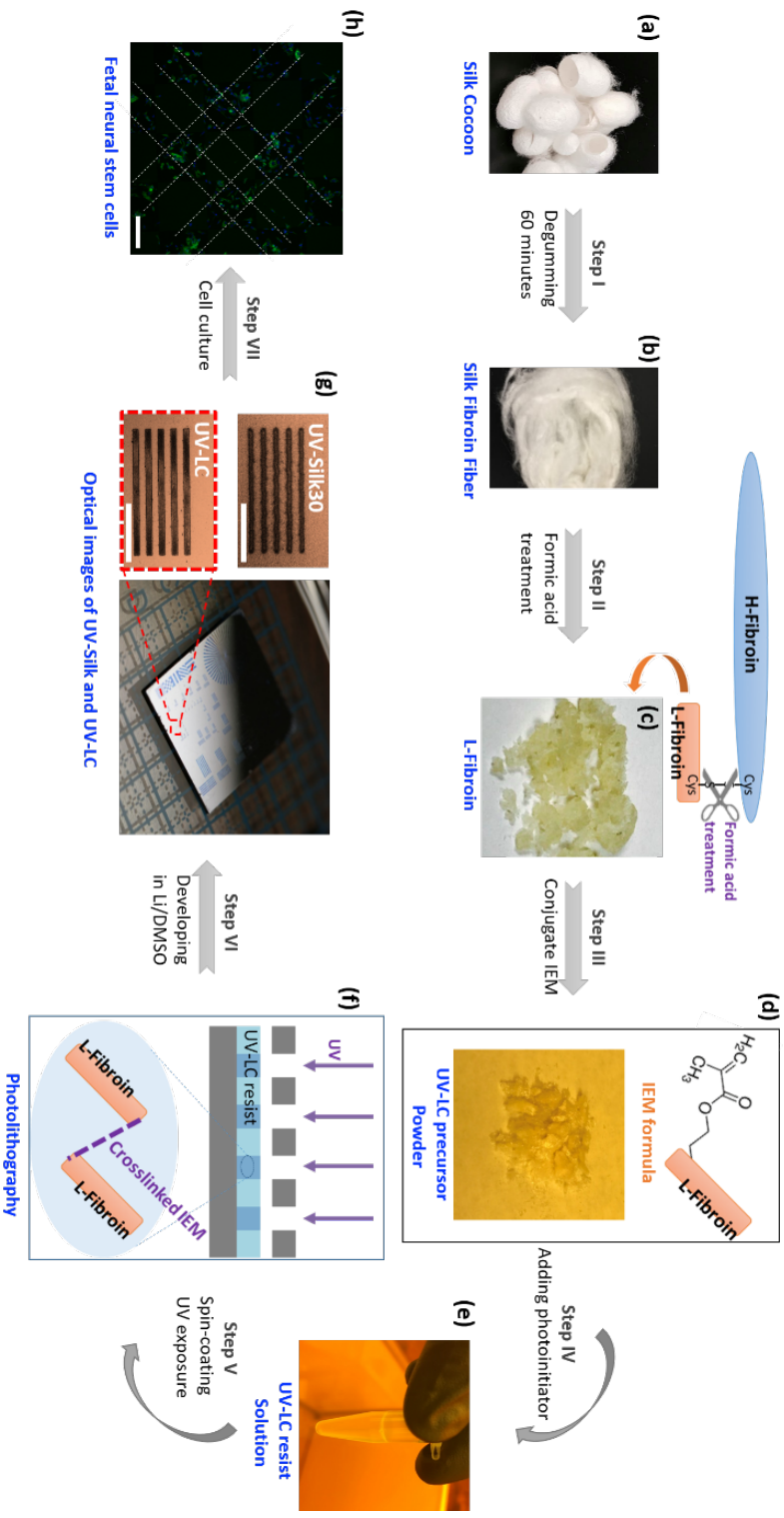
(a)
Silk Cocoon
Step I
Degumming
60 minutes
(b)
Silk Fibroin Fiber
Step II
Formic acid
treatment
(c)
L-Fibroin
Step III
Conjugate IEM
(d)
IEM formula
L-Fibroin
UV-LC precursor
Powder
Step IV
Adding photoinitiator
(e)
UV-LC resist
Solution
Step V
Spin-coating
UV exposure
(f)
UV
UV-LC resist
L-Fibroin
Crosslinked IEM
L-Fibroin
Photolithography
Step VI
Developing
in LI/DMSO
(g)
UV-Silk30
UV-LC
Optical images of UV-Silk and UV-LC
Step VII
Cell culture
(h)
Fetal neural stem cells
H-Fibroin
Cys
Cys
Formic acid
treatment
L-Fibroin

Figure 4.

Figure 4: Synthesis of the UV-reactive silk L-fibroin (UV-LC) and the result of photolithography using UV-LC as a negative resist. B. mori cocoons (a) are degummed for 60 minutes to obtain silk fibroin (b), and the L-fibroin (c) is then separated from the silk fibroin using formic acid; (d) photoactive L-fibroin (UV-LC precursor) is obtained by conjugating IEM to the L-fibroin; (e) by adding the photoinitiator (Irgacure 2959), the UV-LC resist can be synthesized; (f) Photolithography using UV-LC resist; (g) Optical images of the fabricated patterns (Linewidth: 5 μm, zoom-in image) shows that UV-LC has better lithographic performance than UV-Silk30. Scale bar: 50 μm. (h) Dark-field stereomicroscopic photograph of double immunofluorescence staining with nestin (green fluorescence) and nuclear staining (blue DAPI staining) of fetal neural stems cells that were guided to be cultured on a micropatterned UV-LC resist (dash line) on a silicon substrate. Scale bar: 100 μm.

To determine the solvent candidates, solubility was initially investigated to facilitate analysis of the fabrication process. Native silk fibroin protein displays limited solubility when extracted from silk fiber, owing to its secondary structural content. But, with the increase of degumming time, the silk fibroin proteins display enhanced solubility (Figure 5) due to the shorter protein chain length. In addition, the silk fibroin protein preliminary dissolution in salt solution, a process which 'activates' the fibroin. Alcohols are known to follow a trend of protein solubilization: HFIP > trifluoroethanol (TFE) > isopropanol > ethanol > methanol, where the fluorinated alcohols HFIP and TFE are specifically known to enhance solubility thorough stabilization of the α-helical conformation. Furthermore, the solubility of silk fibroin protein in non-aqueous solvents DMSO, N,N-dimethylacetamide (DMAc), and N,N- dimethylformamide (DMF) is negligible without the use of salts to disrupt hydrogen bonding. With the chemical conjugation described, the solubility characteristics of the silk fibroin protein varied

significantly since the added groups present hydrophobic alkene and carbonyl groups at modified amino acids which were occupied via the conjugation reaction. Among the above organic solvents, HFIP was the only solvent to provide solubility and was thus used as a carrier for characterization as well as deposition of photoresists. Thus, HFIP was used as the primary carrier of the photoresist for incorporation into later photolithography steps.

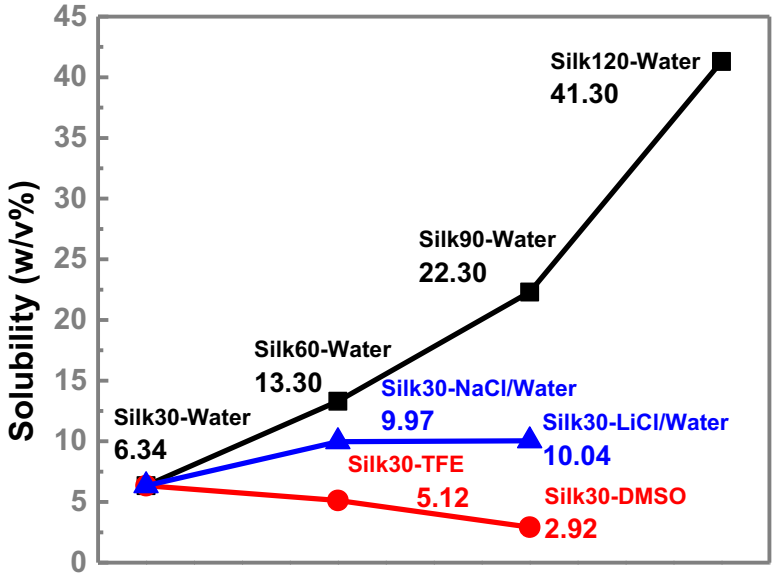

Figure 5: Solubility measurement of silk fibroin proteins under 10, 30, 60, 90 minutes degumming time in different solvents including water, water with salts, TFE and DMSO.

An organic photoinitiator of Irgacure 2959 (Sigma Aldrich, St. Louis, MO) was added 0.5% (w/v) into the UV-LC precursor solution to generate (and transfer) reactive species (free radicals in this case) when exposed to UV radiation (Figure 4e). The UV-LC resist solution (2%, w/v) was spin coated on a silicon or glass substrate to form a resist

layer with a controllable thickness ranging from 50 nm to several μm which was then exposed through a photomask (Figure 4f). In this case, the UV-LC resist acted as a negative photoresist which can be crosslinked due to IEM in the presence of UV light (followed by the development step) to generate wafer-scale micropatterns on silicon and glass substrates via standard UV photolithography (Figure 4g). UV-LC microstructures were tested as cellular substrates and for the spatial guidance of fetal neural stems cells which were seeded on micropatterned surfaces and incubated for 2 days. Cells tended to preferentially attach to the UV-LC protein patterns in comparison to the surrounding surface (i.e., silicon in this case) (Figure 4h). Note that the sensitivity of UV-LC resists can be readily tuned by regulating the IEM molecules conjugated into L-fibroin. Additionally, the presence of unmodified amino acids can enable further functions (e.g., association with favorable cellular interactions and the production of multifunctional biomaterial architectures) via concurrent or subsequent modification strategies [29]. In this study, the IEM molecules were intentionally designed to exceed the population of available amino acids conversion to fully occupy nearly all active group sites on the protein chains to better investigate the underlying mechanism of photo-only-induced formation of crosslinked silk micro-/nano structures.

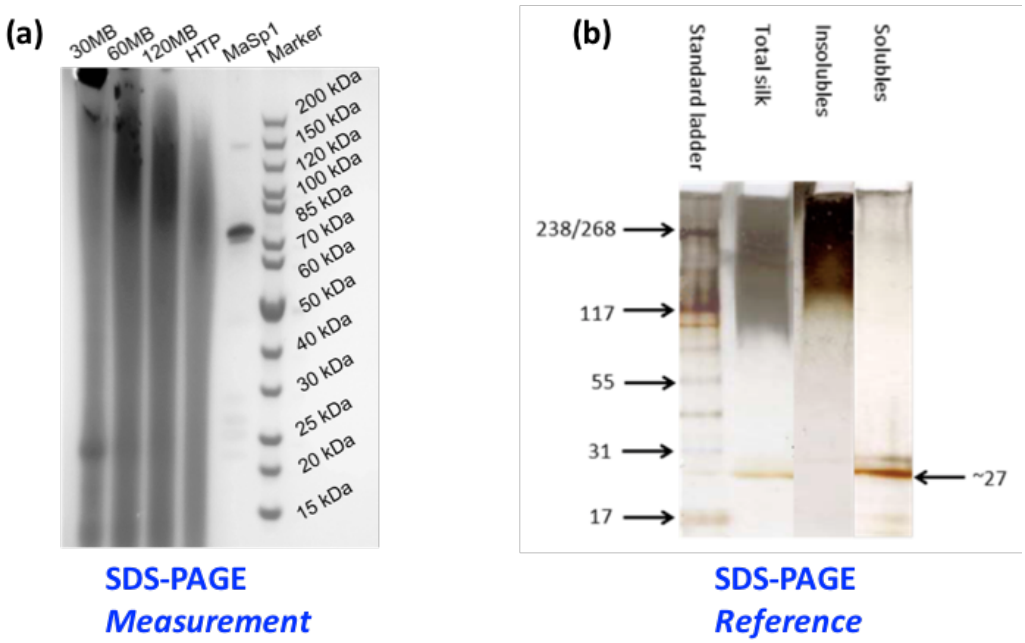

Figure 6: (a) SDS-PAGE analysis of the silk fibroin protein with different degumming time, MaSp1: recombinant spider silk protein; (b) SDS-PAGE analysis of the silk fibroin protein and L-Fibroin from reference [18].

A variety of photoreactive fibroin (UV-Silk) resists with varied degumming conditions (thus varied protein chain lengths and molecular weight distributions) have been prepared for comparison using a previously reported method [17]. Note that UV-Silk resists consist of both H-fibroin and L-fibroin fragments, while UV-LC only has L-fibroin which possesses uniform molecular weight (Figure 6). Figure 7 schematically shows the (simplified) molecular structures of some example UV-Silk and UV-LC precursors, including UV-Silk made of silk fibroin fibers degummed for 30 minutes (UV-Silk30), degummed at high temperature (121 ºC) and pressure (25 psi) for 4 hr (UV-SilkHTP), and L-fibroin protein, respectively. In general, longer degumming time results in shorter but

more uniform silk fibroin fragments. Therefore, compared to UV-Silk30, the H-fibroin fragments in UV-SilkHTP are generally shorter but more uniform due to the high temperature and pressure treatment conditions during its extended degumming process [30]. In comparison, UV-LC provides a promising route serving as the basic molecular blocks for precise protein photolithography thanks to its well-defined and evenly distributed protein chains.

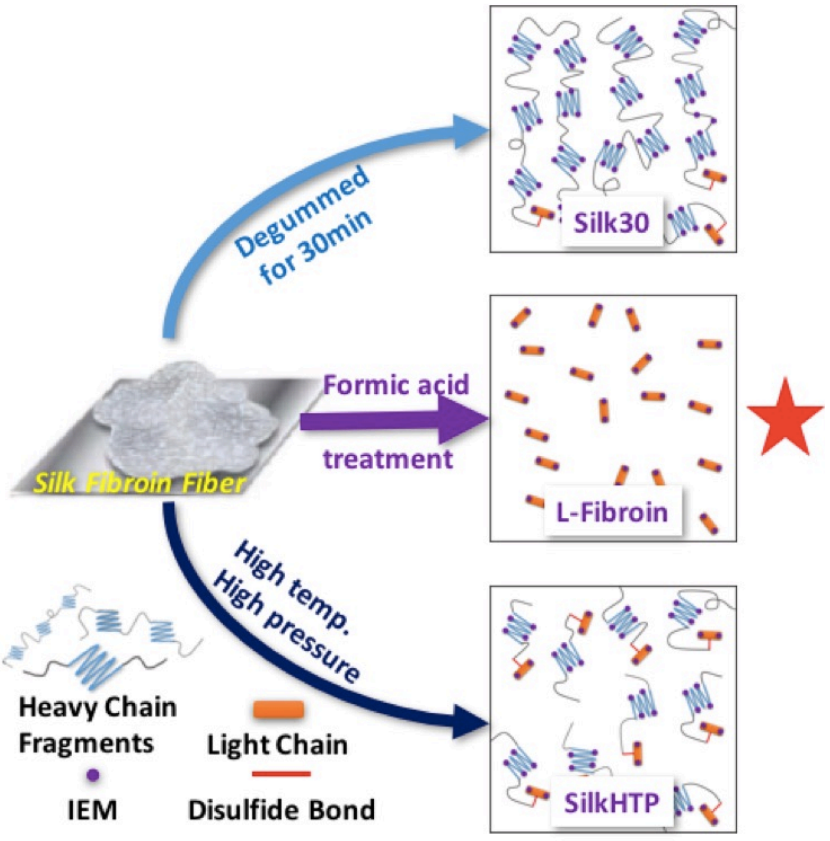

Figure 7: Schematic comparison between structures of UV-LC and UV-Silk (including both UV-Silk30 and UV-SilkHTP) precursor, where UV-Silk30 has longer protein chains than UV-HTP. UV-LC contains only L-fibroin.

CHARACTERIZATION OF THE UV-SILK AND UV-LC MICROPATTERNS

The surface morphology and fidelity of as-fabricated micropatterns on isopropyl alcohol (IPA) cleaned silicon substrates using UV-LC and UV-Silk protein resists were characterized and compared using Atomic Force Microscopy (AFM) and an optical microscope, showing that lithographic performances including the spatial resolution, pattern sharpness, and surface morphology/roughness strongly depend on the molecular structures of as-used protein resists (Figure 8). AFM results show that UV-LC has the best surface roughness with a root mean square (RMS) roughness of ~ 2.3 nm while UV-SilkHTP (~ 8.5 nm) is better than UV-Silk30 (~ 23.8 nm), over an area of 5 × 5 μm. We postulate that, during drying, silk fibroin proteins spontaneously form micro- and nano-scale wrinkled patterns guided by a diffusion-limited aggregation process (DLA) [31] which has been observed in the assembly of a range of materials including colloids, polymer thin films, [32] peptides [33, 34], and proteins [35]. This is partially due to the polarity mismatch between photoreactive silk resists consisting of strongly polar side groups, such as hydroxyl, carboxyl, and amino groups (thus strongly polar) and the IPA-treated silicon (weakly polar) substrate, which can be improved by appropriate surface treatment of silicon substrates.

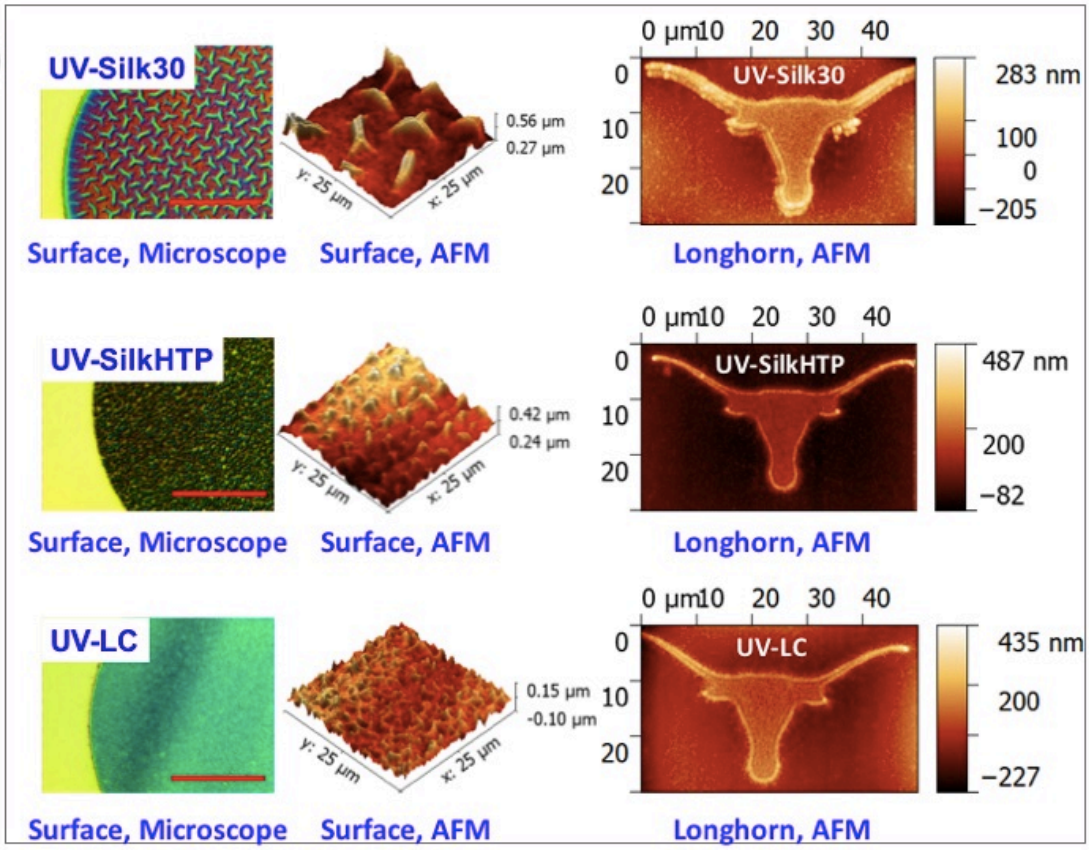

Figure 8: Characterization and analysis of patterns fabricated by protein photolithography using different types of silk-based materials (e.g. UV-Silk30, UV-SilkHTP, and UV-LC. Morphological characterization (using an optical microscope and AFM, scale bar: 200 µm) of micropatterns fabricated by protein photolithography using UV-Silk30, UV-SilkHTP, and UV-LC. It shows that the UV-LC can achieve better resolution and surface smoothness than UV-Silk30 and UV-SilkHTP.

To prove that the formation of wrinkled patterns was attributed to the physical phenomenon but not the secondary structure change, the s-SNOM was employed to measure the absorbance and reflection spectrum of the silk film. According to the properties of s-SNOM, if the chromatic difference at 1,631 cm^{-1} (characteristic peak of the

secondary structure corresponding to the beta sheet) exists along with the height on the surface, the form of wrinkled patterns is resulted from the secondary structure change. Figure 9(b) indicates the AFM image, and the s-SNOM images of both absorbance and reflection spectrum on the surface of UV-silk30 pattern. No contrast difference in the absorbance and reflection images at 1,635 cm^{-1} was observed, which was attributed to the secondary structure at different regions on the surface were basically the same, and only physical phenomenon existed in the self-assembly procedure depending on properties such as particle size, dispersity and charge. The underlying substrate is an important factor that may direct the nature of self-assembly of silk fibroin protein. We initially used silicon as the surface in which the surface was treated by IPA solvent. Due to the more hydrophobicity of silicon with the IPA treatment, the solutions tended to dry unevenly, resulting in aggregated clusters and the formation of a film in many cases (Figure 9). We therefore used the substrate without the IPA treatment in the experiments. The relevant hydrophilic and atomically flat nature of the substrate permitted us to spread the solution and to dry it with smaller concentration gradients, yielding high-resolution AFM images. In addition, the lyophilization process did not change the behavior of silk fibroin protein.

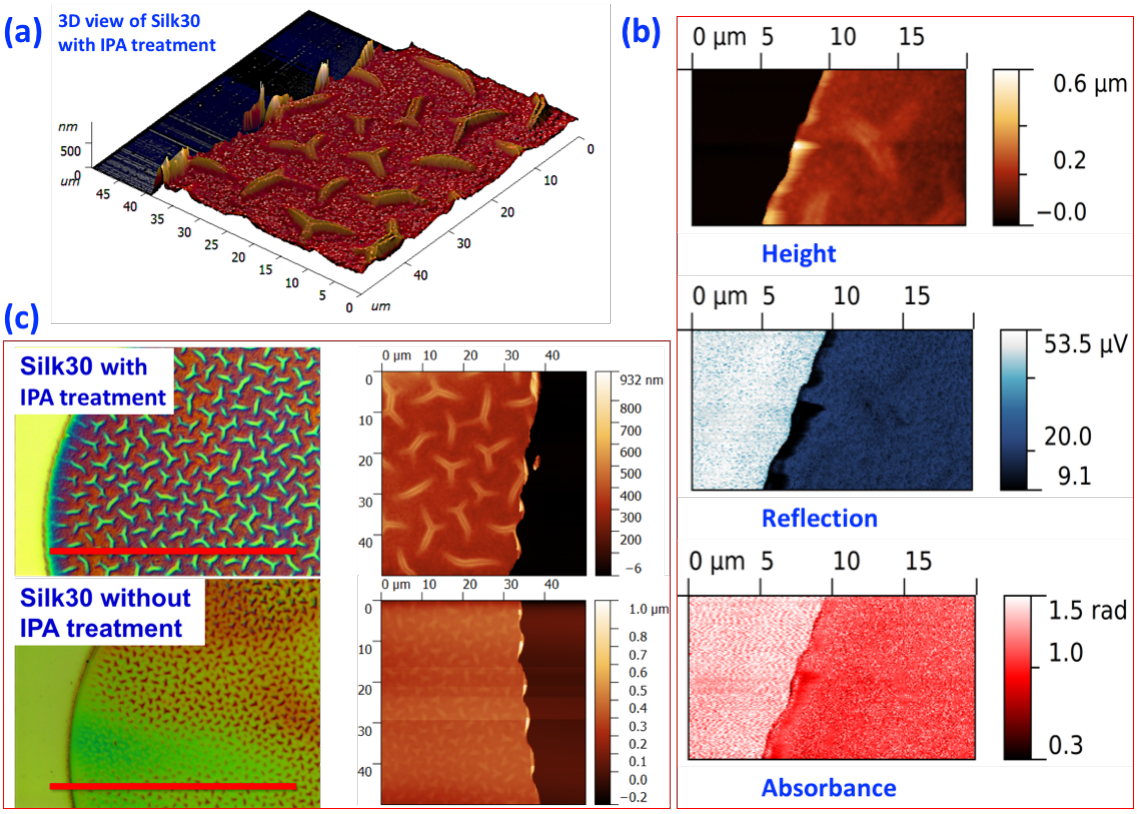

Figure 9: (a) AFM image of 3D view of the surface of silk fibroin protein under 30 minutes degumming time; (b) AFM image and SNOM images of both absorbance and reflection spectrum of the surface of silk fibroin protein under 30 minutes degumming time; (c) Microscope and AFM images of the silk fibroin protein under 30 minutes degumming time to compare the influence of underlying substrate.

The mismatch increases with the protein chain length and uneven distribution of the molecule weight where the internal molecular polarity difference within the protein chain becomes more predominant due to increased ratio between the hydrophobic H-

Fibroin fragments and the hydrophilic L-Fibroin fragments. Figure 10 shows that, under the same lithographic conditions (i.e., exposure duration and development time), the resolution (which was determined by the minimum distinguishable feature size in our case, see the Supplemental Information) of UV-Silk resists improves with the increasing degumming time, due to the decreased (and more uniformly distributed) molecular weight. The UV-SilkHTP and UV-LC provide better lithographic performances in terms of resolution, yielding minimum feature sizes of 1.54 and 1.51 μm, respectively, close to the minimum designed feature size of the mask (1.5 μm), which was chosen based on the capabilities of our current photolithography setup.

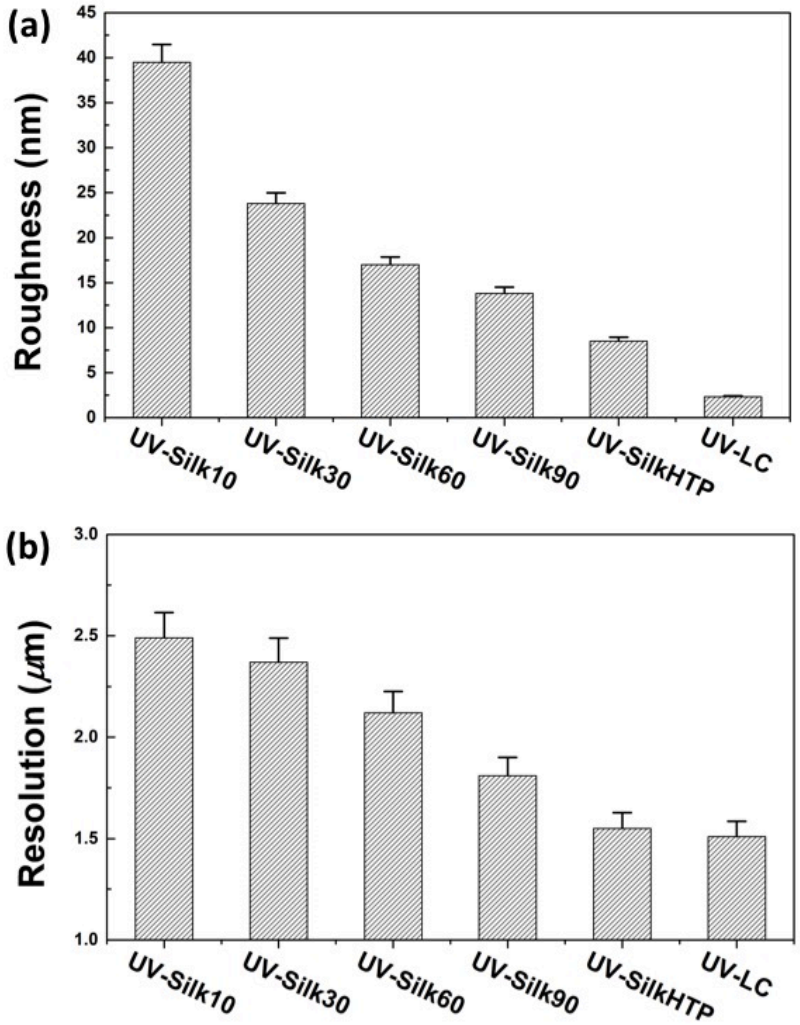

Figure 10: Quantitative analysis of resolution (a) and surface roughness (b) of micropatterns fabricated using various UV-Silk and UV-LC. The result is consistent with the observations from optical and AFM images.

CROOSLINKING MECHANISM ANALYSIS OF THE MICROPATTERNS

The underlying crosslinking mechanism via the conjugation of the multifunctional acrylate moiety (i.e., IEM in this case) to silk fibroin proteins (including both H-fibroin

and L-fibroin) and L-fibroin only - at macro and nano-scale - was investigated via both Fourier transform infrared spectroscopy (FTIR) and the scattering-type scanning near-field optical microscopy (s-SNOM), respectively. Cast films (5.0 mg) were analyzed in attenuated total reflectance (ATR) mode using a Ge ATR crystal, and data was collected between 4000 – 1000 cm^{-1}, for 32 scans at a resolution of 1 cm^{-1}. Here, comparison of spectra to that of the IEM, demonstrates functionalization of IEM to different silk fibroin protein under 10, 30, 60, 90 minutes degumming time, as well as, the silk fibroin protein with high temperature and pressure and L-Fibroin protein. Native silk fibroin under 10, 30, 60, 90 minutes degumming time shows intrinsic Amide I/II/III signals (Figure 11a), which are simultaneously observed for the silk fibroin protein photoresist. The IEM reagent (Figure 11b) shows stretching vibrations at 1720 cm^{-1}, representing carbonyl ester C=O, and 1640 cm^{-1}, assigned to vinyl C=C (which confers photoreactivity), and an additional intense peak is present at 1160 cm^{-1}, resulting from CH_3 rocking vibrations. The silk fibroin protein photoresist under 30 minutes degumming time also shows peaks representing an ester carbonyl, terminal C=C stretching vibrations as broad shoulder peaks of Amide I, and CH_3 rocking vibrations, all provided by the methacrylate group. The absence of this isocyanate stretching vibration from the product indicates the absence of residual isocyanate. The clear observation of characteristic IEM groups in the product provides evidence to support the successful grafting of IEM onto the silk fibroin protein. In addition, no obvious enhancement of methacrylate group peak with an increase of IEM ratio during the fabrication of silk fibroin photoresists (Figure 1b). The secondary structural content of the polypeptide backbone remains relatively unchanged with the methacrylate

bioconjugation reaction. This phenomenon was also observed in UV-SilkHTP and UV-LC. Three characteristic peaks (red curve, Figure 12a) were found in Amide I (1,600 ~ 1,700 cm^{-1}), Amide II (1,500 ~ 1,600 cm^{-1}), and Amide III (1,200 ~ 1,300 cm^{-1}) bands for bulk silk fibroin proteins measured by FTIR in the attenuated total reflection (ATR) mode with an aperture size of several tens of microns, which gradually decreased after the introduction of the photoactive component IEM. Three prominent peaks (blue and pink curves for UV-Silk and UV-LC, respectively) surged at 1,720 cm^{-1} (C=O stretch), 1,635 cm^{-1} (terminal C=C stretch) and 1,160 cm^{-1} (C–O stretch), which overlapped with the characteristic peaks of pure IEM.

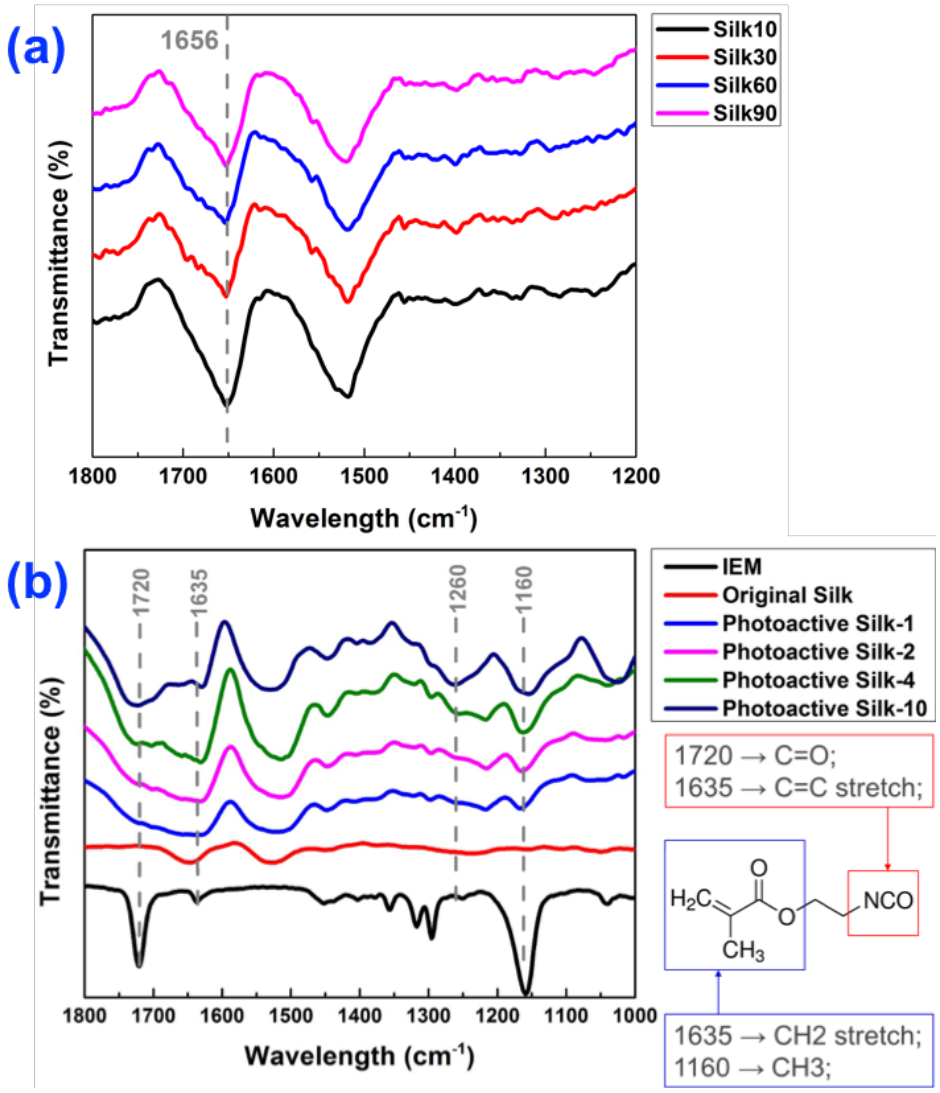

Figure 11: FTIR spectroscopy on the silk fibroin proteins confirms the presence of both amide I/II/III peaks from native silk fibroin proteins, in addition to stretching vibrations at 1720 cm-1 (ester carbonyl C=O) and 1630 cm-1 (vinyl C=C), and vibrations at 1160 cm-1 (CH3) from the methacrylate substituent.

s-SNOM was employed to provide direct imaging and chemical identification of the thin protein layers at the nanoscale, to understand the variation of local chemical

composites during crosslinking under UV exposure, and to overcome the special resolution and thickness limits of FTIR spectroscopic study [36]. In this work, s-SNOM (NeaSNOM, Neaspec GmbH, Germany) has been utilized for high-resolution optical images and spectroscopic information to map out the chemical and mechanical properties of protein patterns at the nanoscale with a spatial resolution of ~ 20 nm. In our setup, s-SNOM is coupled to a tunable IR quantum cascade laser (QCL, Daylight Solutions Inc., USA) covering the broad IR spectra of the Amide I and II bands over the range from 1,450 to 1,750 cm^{-1} (Figure 12c). The near-field phase spectrum resembles the molecular absorbance band, while the near-field amplitude spectrum acquires a dispersive line shape similar to a far-field reflectivity spectrum [37].

Absorbance phase images of UV-Silk30, UV-Silk90, UV-SilkHTP, and UV-LC patterns on a silicon substrate were captured at 1,635 cm^{-1}, which confers IEM-induced photocrosslinking from terminal C=C group sites, where the absorbance intensity is inversely proportional to the degree of crosslink. As shown in Figure 12d, at 1,635 cm^{-1}, the phase image exhibited a strong contrast between silk and silicon (silicon is used as the reference for IR imaging) in UV-Silk30 micropatterns that were exposed for 20 s. The contrast gradually weakened with the longer exposure time indicating an increased crosslinking degree. IEM-induced crosslinking degrees within various protein micropatterns were obtained and evaluated quantitatively (Figure 12e). The absorbance intensity of UV-Silk30 samples decreased monotonically with increasing exposure time until 90 s, indicating an increase in crosslinking degree due to IEM. The crosslinking was found to be saturated after 90 s exposure which expended all available active conjugated

acrylate group sites and remained nearly constant thereafter. It is found that UV-Silk resists with lower molecular weights are easier to crosslink partially due to their higher degrees of molecular mobility and more uniform protein chain lengths. Compared to UV-Silk resists, UV-LC resist shows considerably higher sensitivity thanks to its shorter protein chain length and more available IEM side groups.

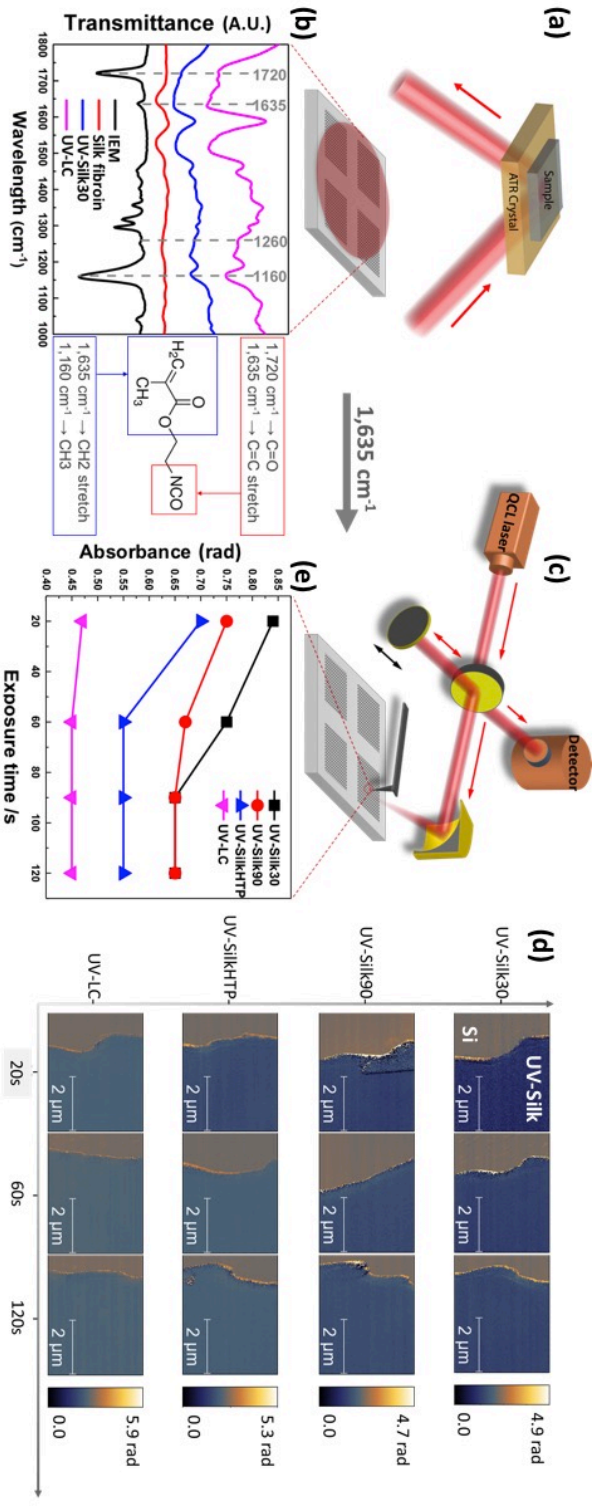
(a)
Sample
ATR Crystal
(b)
Transmittance (A.U.)
Wavelength (cm-1)
1720
1635
1260
1160
IEM
Silk fibroin
UV-Silk30
UV-LC
1,720 cm-1 → C=O
1,635 cm-1 → C=C stretch
1,635 cm-1 → CH2 stretch
1,160 cm-1 → CH3
NCO
1,635 cm-1
(c)
QCL laser
Detector
(d)
UV-Silk30-
UV-Silk90-
UV-SilkHTP-
UV-LC-
UV-Silk
Si
2 μm
4.9 rad
0.0
4.7 rad
5.3 rad
5.9 rad
20s
60s
120s
(e)
Absorbance (rad)
Exposure time /s
UV-Silk30
UV-Silk90
UV-SilkHTP
UV-LC

Figure 12.

Figure 12: Structural characterization of the UV-Silk and UV-LC using FTIR and s-SNOM. (a) Schematic of ATR-FTIR setup, where the sample is illuminated from the back of the ATR crystal; (b) FTIR spectrum of IEM, silk fibroin protein, UV-silk, and UV-LC. The peaks vanish in the UV-Silk and UV-LC, indicating the binding of IEM on silk fibroin and L-fibroin; (c) Schematic of the s-SNOM system. An infrared laser is focused onto the AFM tip, and the scattered signal is collected by the detector; (d) & (e) IR nano-imaging and absorbance (acquired by s-SNOM measurement performed at 1,635 cm-1) of UV-Silk30, UV-Silk90, UV-SilkHTP and UV-LC with various exposure time. The disappearance of the absorbance with increasing exposure time indicates the increasing crosslinking degree of IEM until about 90 s, after which time all the available IEM active conjugated acrylate group sites are crosslinked.

ETCHING RESISTANCE MEASUREMENT AND ANALYSIS OF THE MICROPATTERNS

One main use of photolithography is to pattern a resist layer which can serve as a temporary mask when etching an underlying layer. Therefore, a systematic study on the use of UV-Silk and UV-LC resists as the etching mask for pattern transfer was conducted. We've found that there are at least three factors that play an important and synergistic role in the etching performance (i.e., etching resistance) of the silk-based microstructures, namely:

1) The average molecular weight (i.e., average protein chain length, which is determined by the degumming process (for UV-Silk resists) and protein separation process (for UV-LC resist));

2) The photoinduced crosslinking due to IEM;

3) The crosslinking due to the formation of beta sheets.

We first investigated the dependence of etching performance on the photoinduced

crosslinking within the protein matrix and the protein chain lengths. As shown in Figure 13a, the etching rates of both UV-Silk30 and UV-LC resists decreased monotonically with the increased exposure time (and thus the increased crosslinking degree before saturation) and reached plateaus at ~ 25.4 nm/min and ~ 72.4 nm/min after UV exposure of 90 s and 30 s, respectively. The etching resistance of UV-LC was initially better than UV-Silk30 since the crosslinking degree in UV-LC was considerably higher than UV-Silk30 under the same exposure conditions. With the increased exposure time, the molecular weight of silk protein chains became to play a more important role and UV-Silk30 showed a better etching resistance when both resists were fully crosslinked.

We designed two sets of experiments to systematically investigate the etching performance among a variety of silk resists (including both UV-Silk and UV-LC ones) that were 1) partially crosslinked (for 20 s exposure so that all resists were "under-exposed") and 2) fully crosslinked (for 120 s exposure so that all resists were 'over-exposed') (Figure 13b). It has been found that, under same exposure conditions (for both partially and fully crosslinking cases), the etching rate of UV-Silk resists increased with the degumming time. This is mainly due to the reduced protein chain length during the prolonged degumming process which weakens the mechanical strength of the as-prepared protein resist and causes the increase in the etching rate (Figure 13c). A schematic illustration of the underlying mechanism is given in Figure 13d. We then compared the etching performances of UV-LC resist to UV-Silk ones. In the partially crosslinking case, the UV-LC resist showed the best etching performance due to its significantly higher crosslinking degree than all UV-Silk resists (also see Figure 13e). However, for the fully crosslinking case, a competing

mechanism becomes more noticeable between the crosslinking degree and the molecular weight on the etching performance. Generally, UV-LC resist has much lower molecular weight but higher crosslinking degree than UV-Silk resists under same exposure conditions. Therefore, when fully crosslinked, UV-Silk resists with relatively short degummed time showed better etching resistance than UV-LC, due to their much higher molecular weights and better mechanical strengths. UV-Silk90 shows a comparable etching resistance to UV-LC as it has higher molecular weight but less crosslinking degree. UV-SilkHTP shows the highest etching rate as it has much lower average molecular weight than other UV-Silk counterparts due to the excessive degumming time under high temperature and pressure.

Furthermore, we've found that the influence of the secondary structure of beta sheets within silk resists on their etching performances is considerably minor compared to the other two factors, namely, the average molecular weight and IEM-induced crosslink. It is well known that methanol treatment can promote the formation of beta sheets within the silk protein matrix [6]. No noticeable variation was found in terms of the etching resistance before and after the methanol treatment for all silk resist samples (Figure 13b). We attribute this to the fact that the degree of IEM substitution was designed to exceed the population of amino acids conversion so to occupy almost all the active group sites on the protein chains, which hindered the formation of betasheet structures in the protein resist matrix.

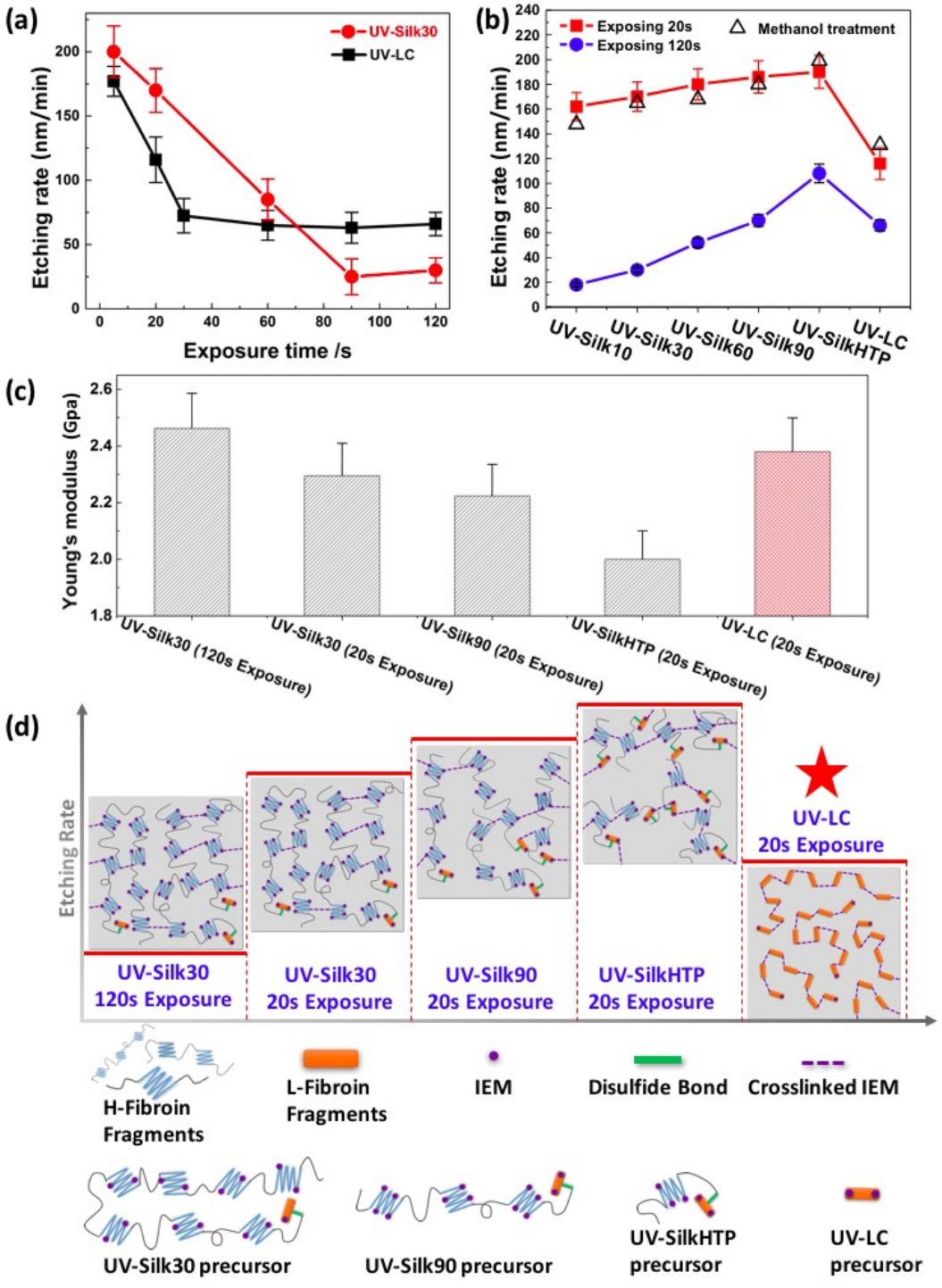
(a)
UV-Silk30
UV-LC
Etching rate (nm/min)
Exposure time /s
(b)
Exposing 20s
Exposing 120s
Methanol treatment
Etching rate (nm/min)
UV-Silk10
UV-Silk30
UV-Silk60
UV-Silk90
UV-SilkHTP
UV-LC
(c)
Young's modulus (Gpa)
UV-Silk30 (120s Exposure)
UV-Silk30 (20s Exposure)
UV-Silk90 (20s Exposure)
UV-SilkHTP (20s Exposure)
UV-LC (20s Exposure)
(d)
Etching Rate
UV-Silk30 120s Exposure
UV-Silk30 20s Exposure
UV-Silk90 20s Exposure
UV-SilkHTP 20s Exposure
UV-LC 20s Exposure
H-Fibroin Fragments
L-Fibroin Fragments
IEM
Disulfide Bond
Crosslinked IEM
UV-Silk30 precursor
UV-Silk90 precursor
UV-SilkHTP precursor
UV-LC precursor

Figure 13.

Figure 13: Etching rate measurements and schematic structures of various UV-Silk and UV-LC. (a) Etching rate measurement of the UV-Silk30 and UV-LC with increasing exposure time. The etching rate of UV-LC decreases faster than the UV-Silk30 with increasing exposure time but reaches a constant rate that is higher than UV-Silk30; (b) Etching rate comparison between various UV-Silk (including both UV-Silk and methanol treated UV-Silk) and UV-LC at two exposure times (20s and 120s). All the samples with 20 s exposure times have larger etching rate than the samples with 120 s exposure times. UV-Silk has an increasing etching rate with increasing degumming time because the mechanical strength is better with longer chain length. UV-LC has slightly less etching rate because its highly defined molecular structure help form better crystalline structure; (c) Young's modulus of UV-Silk and UV-LC. It shows the similar trend with the data of etching speed, where the largest Young's modulus value corresponds to slower etching rate; (d) Schematic structure and the corresponding etching rate of the photocrosslinked UV-Silk and UV-LC with 20 s exposure time and UV-Silk30 exposed for 120 s. For UV-Silk30, the etching rate decreases with longer exposure time because of the increased crosslinking degree. With the same exposure time, the etching rate increases with increasing degumming time because of the shorter chain length, and thus less mechanical strength. With 20 s exposure (partially crosslinking) UV-LC has less etching speed because its highly defined molecular structure helps it form better IEM-induced crystalline structure.

BIOCOMPATABILITY AND CELL CULTURE ANALYSIS OF THE MICROPATTERNS

One of the most compelling attributes of silk materials is their abilities to allow for the incorporation of functional elements such as labile biological components with retention of bioactivity to generate functional material formats. The effectiveness of UV-LC photolithography to large scale reproduce microscale geometries and topologies allows for functional components to be generated from silk. We therefore explore the doping and stabilization of UV-LC patterns with an enzyme of horseradish peroxidase (HRP) and the effects of the UV-LC photolithography process on its bioactivities as proof-of-principle demonstrations. As shown in Figure 14a and b, the enzymatic activity of the HRP-doped

UV-LC resist was assessed by a colorimetric enzyme-linked immunosorbent assay (ELISA) for HRP/ 3,3′,5,5′-tetramethylbenzidine (TMB) after UV exposure and pattern development. The bioactivity test shows that as-prepared patterns possess bioactivity of embedded biological molecules to some extent (i.e., HRP-dope UV patterns turn blue after exposure to TMB) during UV-LC photolithography. Finally, UV-LC microstructures were fabricated and examined using a standard immunofluorescence assay as biocompatible cellular substrates (Figure 14c – 14e). Fetal neural stem cells were seeded on non-patterned (i.e., a uniform coating of UV-LC resist w/o UV exposure) and patterned surfaces using UV-LC photolithography and incubated for 3 days. As shown in Figure 14f and g, cells were well anchored to the UV-LC substrates in both cases and tended to preferentially attach to UV-LC patterned compared to the surrounding surface (i.e., silicon in this case), showing that UV-LC micropatterns have good biocompatibility and can be used for precisely spatial cell guidance.

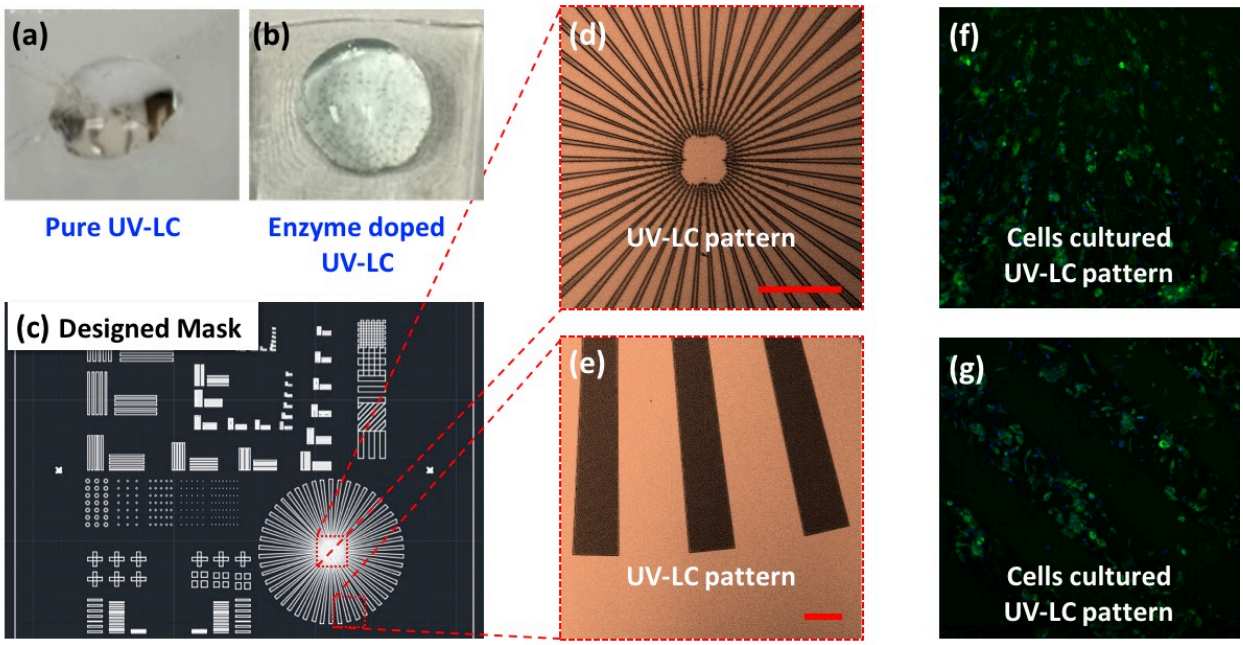

Figure 14: (a) and (b) Bioactivity detection (ELISA) of pure silk resist and HRP enzyme doped silk resist (which turns blue) after UV exposure and pattern development. The bioactivity test shows that as-prepared patterns possess bioactivity of embedded biological molecules to some extent during silk light chain protein photolithography; (c)-(g) Double immunofluorescence staining with nestin (green fluorescence) and nuclear staining (blue DAPI staining) of fetal neural stem cells cultured on micropatterns made of silk light chain photolithography.

Chapter 5: Conclusion

In conclusion, we report on a precise protein photolithography (P^3) for wafer-scale, high-performance biopatterning using chemically modified well-defined silk L-fibroins as the photoresist material. The lithographic and etching performance of UV-LC and UV-Silk resists have been evaluated systematically and the underlying mechanisms have been thoroughly discussed. A general guidance on the synthesis and the use of silk L-fibroin resist has been provided. The inherent biocompatibility and the enhanced patterning resolution along with the improved surface roughness and etching performance of such protein-based resists offer new opportunities in fabricating large-scale high-precision biocompatible functional micro-/nano structures.

This work describes a technical advance of the scattering-type or apertureless SNOM. We used such technique to prove that the winkle structure on the UV-Silk30 pattern was a sort of self-assembly which a physical phenomenon. Also, we measure the variation of the crosslinking degree in the protein matrix with the exposure time under UV light. Such local probe technique can provide direct imaging and chemical identification of the thin protein layers at the nanoscale, to understand the variation of local chemical composites of biomaterials, and to help biomanufacturing technique to a breakthrough in applications.

References

[1] Pritchard, E. M., & Kaplan, D. L. (2011). Silk fibroin biomaterials for controlled release drug delivery, Expert Opinion on Drug Delivery, 8, 797-811.

[2] Hwang, S. W., Tao, H., Kim, D. H., Cheng, H., Song, J. K., Rill, E., Brenckle, M. A., Panilaitis, B., Won, S. M., Kim, Y. S., Song, Y. M., Yu, K. J., Ameen, A., Li, R., Su, Y., Yang, M., Kaplan, D. L., Zakin, M. R., Slepian, M. J., Huang, Y., Omenetto, F. G., & Rogers, J. A. (2012). A physically transient form of silicon electronics, Science, 337, 1640-1644.

[3] Tao, H., Kaplan, D. L., & Omenetto, F. G. (2012). Silk Materials – A Road to Sustainable High Technology, Advanced Materials, 24, 2824-2837.

[4] Omenetto, F. G., & Kaplan, D. L. (2010). New opportunities for an ancient material, Science, 329, 528-531.

[5] Vollrath, F., & Knight, D. P. (2001). Liquid crystalline spinning of spider silk, Nature, 410, 541-548.

[6] Lu, Q., Hu, X., Wang, X., Kluge, J. A., Lu, S., Cebe, P., & Kaplan, D. L. (2010). Water-insoluble silk films with silk I structure, Acta Biomaterialia , 6, 1380-1387.

[7] Drachuk, I. (2015). Silk Macromolecules With Amino Acid-Poly(ethylene Glycol) Grafts for Controlling Layer-By-Layer Encapsulation and Aggregation of Recombinant Bacterial Cells, ACS Nano, 9, 1219-1235.

[8] Mandal, B. B., & Kundu, S. C. (2009). Cell proliferation and migration in silk fibroin 3D scaffolds, Biomaterials, 30, 2956-2965.

[9] Galeotti, F., Andicsova, A., Yunus, S., & Botta, C. (2012). Precise surface patterning of silk fibroin films by breath figures, Soft Matter, 8, 4815-4821.

[10] Altman, G. H., Diaz, F., Jakuba, C., Calabro, T., Horan, R. L., & Chen, J. (2003). Silk-based biomaterials, Biomaterials, 24, 401-416.

[11] Gates, B. D., Xu, Q. B., Stewart, M., Ryan, D., Willson, C. G., & Whitesides, G. M. (2005). New approaches to nanofabrication: molding, printing, and other techniques, Chemical Reviews, 105, 1171-1196.

[12] Geissler, M., & Xia, Y. N. (2004). Patterning: Principles and Some New Developments, Advanced Materials, 16, 1249-1269.

[13] Hengsakul, M., & Cass, A. E. G. (1996). Protein Patterning with a Photoactivatable Derivative of Biotin, Bioconjugate Chemistry, 7, 249-254.

[14] Raphel, J., Parisi-Amon, A., & Heilshorn, S. C. (2012). Photoreactive elastin-like proteins for use as versatile bioactive materials and surface coatings, Journal of Materials Chemistry, 22, 19429-19437.

[15] Carrico, I. S., Maskarinec, S. A., Heilshorn, S. C., Mock, M. L., Liu, J. C., Nowatzki, P. J., Franck, C., Ravichandran, G., & Tirrell, D. A. (2007). Lithographic Patterning of Photoreactive Cell-Adhesive Proteins, Journal of American Chemical Society, 129, 4874-4875.

[16] Kurland, N. E., Dey, T., Wang, C. Z., Kundu, S. C., & Yadavalli, V. K. (2014). Silk Protein Lithography as a Route to Fabricate Sericin Microarchitectures, Advanced Materials, 26, 4431–4437.

[17] Kurland, N. E., Dey, T., Kundu, S. C., & Yadavalli, V. K. (2013). Precise Patterning of Silk Microstructures Using Photolithography, Advanced Materials, 25, 6207-6212.

[18] Zafar, M. S., Belton, D. J., Hanby, B., Kaplan, D. L., & Perry, C. C. (2015). Functional material features of Bombyx mori silk light versus heavy chain proteins, Biomacromolecules, 16, 606-614.

[19] Shimura, K., Kikuchi, A., Ohtomo, K., & Katagata, Y. (1976). Studies on Silk Fibroin of Bombyx mori. I. Fractionation of Fibroin Prepared from the Posterior Silk Gland, Journal of Biochemistry, 80, 693-702.

[20] Tanaka, K., Inoue, S., & Mizuno, S. (1999). Hydrophobic interaction of P25, containing Asn-linked oligosaccharide chains, with the H-L complex of silk fibroin produced by Bombyx mori, Insect Biochemistry and Molecular Biology, 29, 269-276.

[21] Hota, M. K., Bera, M. K., Kundu, B., Kundu, S. C., & Maiti, C. K. (2012). A Natural Silk Fibroin Protein-Based Transparent Bio-Memristor, Advanced Functional Materials, 22, 4493-4499.

[22] Tanakaa, K., Kajiyamaa, N., Ishikuraa, K., Wagaa, S., Kikuchia, A., Ohtomoa, K., Takagib, T., & Mizuno, S. (1999). Biochimica et Biophysica Acta (BBA) - Protein Structure and Molecular Enzymology, 1432, 92-98.

[23] Yamaguchi, K., Kikuchi, Y., Takagi, T., Kikuchi, A., Oyama, F., Shimura, K., & Mizuno, S. (1989). Primary structure of the silk fibroin light chain determined by cDNA sequencing and peptide analysis, Journal of Molecular Biology, 210, 127-139.

[24] Garel, J. (1982). The slow-binding and slow, tight-binding inhibition of enzyme-catalysed reactions, Trends in Biochemical Sciences, 7, 102-105.

[25] Tanaka, K., Inoue, S., & Mizuno, S. (1999). Hydrophobic interaction of P25, containing Asn-linked oligosaccharide chains, with the H-L complex of silk fibroin

produced by Bombyx mori., Insect Biochemistry and Molecular Biology, 29, 269-276.

[26] Rockwood, D. N., Preda, R. C., Yücel, T., Wang, X., Lovett, M. L., & Kaplan, D. L. (2011). Materials fabrication from Bombyx mori silk fibroin, Nature Protocols, 6, 1612-1631.

[27] Wadbua, P., Promdonkoy, B., Maensiri, S., & Siri, S. (2010). Different properties of electrospun fibrous scaffolds of separated heavy-chain and light-chain fibroins of Bombyx mori, International Journal of Biological Macromolecules, 46, 493-501.

[28] Oyama, F. (1984). Studies on Immunological Properties of Fibroin Heavy and Light Chains, Journal of Biochemistry, 96, 1689-1694.

[29] Wong, S. S., & Jameson, D. M. (2012). Taylor & Francis/CRC Press, Boca Raton.

[30] Qin, N., Zhang, S., Jiang, J., Zhou, Z., Xia, X., Tao, H., & Liu, K. (2017). Precise Control of Natural and Synthetic Silk Nanostructures Using Electron Beam Lithography, MEMS Conference.

[31] Witten T. A., & Sander, L. M. (1981). Diffusion-Limited Aggregation, a Kinetic Critical Phenomenon, Physical Review Letters, 47, 1400.

[32] Reiter, G., Botiz, I., Graveleau, L., Grozev, N., & Albrecht, K. (2007). Morphologies of Polymer Crystals in Thin Films, Progress in Understanding of Polymer Crystallization, 714, 179-200.

[33] Lomander, A., Hwang W. M., & Zhang, S. G. (2005). Hierarchical Self-Assembly of a Coiled-Coil Peptide into Fractal Structure, Nano Letter, 5, 1255-1260.

[34] Sneer, R., Weygand, M. J., Kjaer, K., Tirrell D. A., & Rapaport, H. (2004). Parallel beta-sheet assemblies at interfaces, ChemPhysChem, 5, 747-750.

[35] Murr M. M., & Morse, D. E. (2005). Fractal intermediates in the self-assembly of silicatein filaments, Proceedings of the National Academy of Sciences of the United States of America, 102, 11657-11662.

[36] Qin, N., Zhang, S., Jiang, J., Corder, S. G., Qian, Z., Zhou, Z., Lee, W., Liu, K., Wang, X., Li, X., Shi, Z., Mao, Y., Bechtel, H. A., Martin, M. C., Xia, X., Marelli, B., Kaplan, D. L., Omenetto, F. G., Liu, M., & Tao, T. H. (2016). Nanoscale probing of electron-regulated structural transitions in silk proteins by near-field IR imaging and nano-spectroscopy, Nature Communication, DOI: 10.1038/ncomms13079

[37] Brehm, M., Taubner, T., Hillenbrand R., & Keilmann, F. (2006). Infrared Spectroscopic Mapping of Single Nanoparticles and Viruses at Nanoscale Resolution, Nano Letter, 6, 1307-1310.